ACS APPLIED NANO MATERIALS

www.acsanm.org Article

Sputter Gas Damage in Nanolayered Pt/Co/Ir-based Synthetic Antiferromagnets for Top-Pinned Magnetic Tunnel Junctions

Chloe S. Taylor, Marzieh Savadkoohi, Pawan Tyagi, Jenae E. Shoup, Dario A. Arena, Julie A. Borchers, James Eckert, and Daniel B. Gopman*

Cite This: ACS Appl. Nano Mater. 2023, 6, 131−139 Read Online

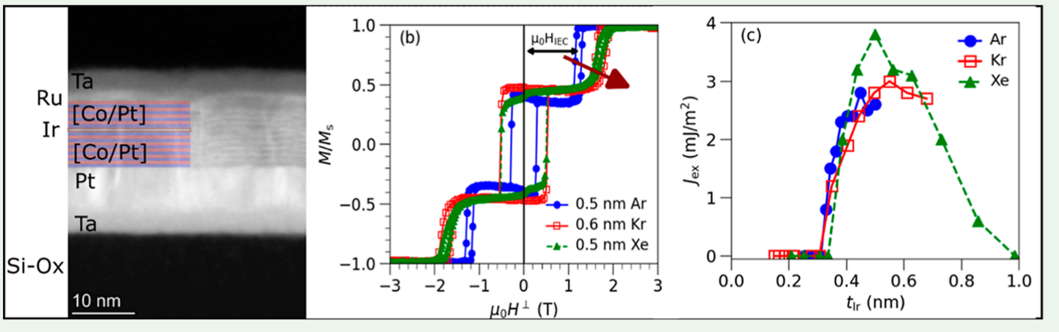

ABSTRACT: We examine the role of sputter damage on limiting the perpendicular magnetic anisotropy and interlayer exchange coupling in Pt/Co/Ir-based synthetic antiferromagnets, a key building block used in the microelectronics community for standalone and embedded magnetic random access memories. By replacing the more conventional Ar process gas with Kr or Xe, we reduce the energy of backscattered sputter gas ions bombarding the substrate from in excess of 100 eV to a few 10 s of eV. Reducing this kinetic bombardment is critical to avoid intermixing of this nanolayered functional heterostructure, with the constituent Pt, Co, and Ir layer thicknesses each below 1 nm. Our approach leads to a simultaneous enhancement in the perpendicular magnetic anisotropy ($>2 \times 10^6$ J/m^3) and interlayer exchange coupling energy (>3.5 mJ/m^2). This advantageous improvement in perpendicular anisotropy and interlayer exchange coupling is evident on a 5 nm-thick Pt buffer layer and additionally on an MgO/CoFeB/Mo underlayers complex, showing that this method can improve the performance of both top- and bottom-pinned reference layers in perpendicular magnetic tunnel junction devices. These experimental findings may help advance the processing of conventional and synthetic antiferromagnetic devices for emerging spintronic memory technologies.

KEYWORDS: *magnetic tunnel junction, perpendicular magnetic anisotropy, synthetic antiferromagnets, sputtering, sputter damage, magnetic multilayers*

I. INTRODUCTION

Significant ongoing research efforts in spintronic applications are focused on the development and processing of synthetic antiferromagnets (SAFs), the trilayered FM1/NM/FM2 structure, where FM is a ferromagnet and NM is typically an ultrathin (<1 nm) nonmagnetic metal that typically includes Cr, Ru or Ir.[1] The interlayer exchange coupling (IEC) across the NM layer shows an oscillatory and decaying behavior that can be ferromagnetic (FM) or anti-FM,[2−4] but the anti-FM behavior is of particular technological interest to spintronic applications as the building block of a fringe-field free reference layer for ultrahigh density spin-transfer-torque magnetic random access memory (STT-MRAM) cells.[5,6] Additionally, the SAF shows technological merit as the free layer for SAF magnetic tunnel junctions (MTJs)[7−9] and as domain wall and Skyrmion bubble devices,[10,11] in which case the IEC torques can generate faster magnetization switching, enable high domain wall velocities, and stabilize Skyrmions at elevated temperature compared to FM counterparts. Furthermore, SAFs are believed to deliver topological protection for energy efficient spin−orbit torque MRAM devices,[12] including protection of chiral Neel-type domain walls in domain wall[13−16] and Skyrmion racetrack memory devices[17] by potentially reducing or eliminating the deleterious Skyrmion Hall effect.[18,19]

Perpendicular magnetic anisotropy (PMA) is of even greater significance to spintronic technologies due to the high-density scaling advantages afforded over in-plane magnetized counter-

Received: September 4, 2022
Accepted: December 7, 2022
Published: December 23, 2022

https://doi.org/10.1021/acsanm.2c03917
ACS Appl. Nano Mater. 2023, 6, 131−139

parts.[20] While a uniaxial PMA can be derived from spin−orbit coupling in the lattice of a FM film, the most technologically relevant materials derive their PMA from the broken symmetry at interfaces in ultrathin nanolayered films, such as NM/CoFeB/MgO or Co/NM multilayers,[21−27] where the nonmagnetic layer and the quality of the interface are both key to realizing a sufficiently large PMA energy density to enable thermally stable nanomagnetic layers with lateral sizes in the 10 s of nm and a sub-10 nm thickness.

Certain technological realizations of SAFs in spintronic applications combine PMA and IEC. This requires certain compromises in materials and functional properties. For instance, while Ru has the largest IEC energy (5 mJ/m^2),[3] it does not contribute significant PMA in Ru/CoFeB/MgO.[28] On the other hand, while Pt/Co multilayers can be engineered with very high PMA (>1 MJ/m^3),[29] Pt does not offer an anti-FM IEC.[30] It was shown that Ir can deliver both high IEC and is compatible with high PMA Co/Pt multilayers for a perpendicular SAF (pSAF) with 2.5 mJ/m^2 IEC energy and 1 MJ/m^3 PMA.[31] This has led to high-tunneling magnetoresistance bottom-pinned perpendicular MTJs (pMTJs) using a pSAF as part of the reference layer coupled to a CoFeB film.[32]

Ultrathin magnetic multilayers including the [Co/Pt]/Ir/[Co/Pt] pSAF are grown by physical vapor deposition sputtering in most conventional research and manufacturing facilities. This industry-friendly approach is high-throughput and scales adequately for back-end-of-line deposition of highly uniform spintronic films across semiconductor wafers, even with the requirement of individual Co, Pt, and Ir layer thicknesses ranging from 0.5 nm and below with lateral thickness homogeneity across 300 mm diameter, manufacturing-scale semiconductor wafers.[25,32] Figure 1a depicts the sputter deposition technique, in which a plasma generated in the vicinity of a biased target leads to energetic bombardment (100 s of eV) of the target by ionized process gas atoms, that eject (sputter) a flux of target atoms and reflected process gas ions toward the substrate. This additional flux from reflected ions can lead to significant energetic bombardment of the growing film during deposition, the extent of which is highly sensitive to process parameters like the sputter gas and target composition, the background gas pressure during deposition, and the distance from substrate to sputtering target.[33] While previous works have reported peak IEC energy as high as 2.6 mJ/m^2 in a [Co/Pt]/Ir/[Co/Pt] pSAF,[31] opportunities remain to realize further gains in IEC and PMA through modification of the processing conditions during sputtering. In particular, previous results showing the gains in coercivity and PMA energy by use of heavier process gases (relative to Ar) during Pt deposition in Co/Pt multilayers.[34,35] Additionally, controlled ion bombardment during ion milling of a similar PMA system, Co/Pd multilayers, has shown that the magnitude of arriving ion energy can significantly modify the PMA, with 10 s of eV having a minimum impact, but higher energies being particular deleterious to the PMA energy.[36] These results taken together suggest a similar approach should be considered for [Co/Pt]/Ir/[Co/Pt] pSAFs, whereby the similar molecular weight of Ir target atoms should also generate significant high-energy bombardment of backscattered Ar$^+$ ions during sputtering.

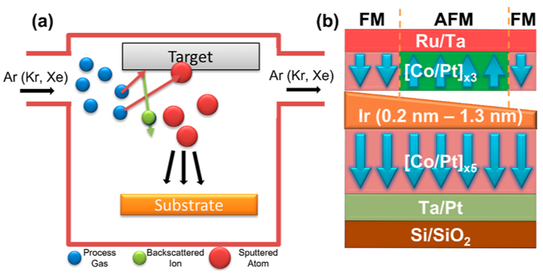

Figure 1. Scheme representing (a) sputter deposition of nanolayered thin films; (b) layer stacking structure and mutual magnetization alignment of $[Co/Pt]_{\times 5}/Ir/[Co/Pt]_{\times 3}$ SAF.

We demonstrate that by replacing Ar with Kr or Xe during the deposition of a [Co/Pt]/Ir/[Co/Pt] pSAF, it is possible to realize gains in three relevant metrics for spintronic applications—the perpendicular coercivity, the PMA energy, and the IEC energy. In particular, we demonstrate the peak IEC coupling in a pSAF sputtered in Xe can exceed 3 mJ/m^2, a significant improvement over an Ar-sputtered counterpart deposited under identical conditions. Furthermore, we demonstrate that the improved functional properties are evident not only in a highly (111) face-centered-cubic textured Pt-buffered pSAFs but also when grown above a Ta/MgO/CoFeB/Mo underlayers structure, indicating compatibility with top-pinned reference layer structures for high-density STT-MRAM. These results highlight the importance of process gas engineering for advanced spintronics technologies.

Thin-film multilayers were produced by magnetron sputtering in a custom ultrahigh vacuum chamber with base pressure less than 6.7 × 10^{-8} Pa (5.0 × 10^{-10} Torr). All metal layers were grown by direct current magnetron sputtering, while the MgO layer was grown by radio frequency sputtering. Two series of samples were grown in this study:

Series A: Si (001) sub./SiO_2 (500 nm)/Ta (5 nm)/Pt (5 nm)/[Co (0.4 nm)/Pt (0.6 nm)] × 5/Co (0.4 nm)/Ir (wedge)/[Co (0.4 nm)/Pt (0.6 nm)] × 3/Ru(2 nm)/Ta(5 nm). Series B: Si(001) sub./SiO_2 (500 nm)/Ta(5 nm)/MgO (2 nm)/CoFeB (1.1 nm)/Mo (0.8 nm)/[Co (0.4 nm)/Pt (0.6 nm)] × 3/Co (0.4 nm)/Ir (wedge)/[Co (0.4 nm)/Pt (0.6 nm)] × 6/Ru (2 nm)/Ta (5 nm).

The layer-stacking structure in series A is an optimized Ta/Pt underlayer sequence for the face-centered-cubic (111) growth of the Pt/Co/Ir-based SAF and is designed as a potential building block for bottom-pinned pMTJs, spin-Hall domain wall devices or Skyrmion devices. Series B places the SAF above a Ta/MgO/CoFeB underlayer sequence with indirect exchange coupling to the CoFeB layer through a thin Mo spacer and serves to evaluate the suitability of this SAF structure as a top-pinning reference layer for pMTJs. While the majority of the layers were grown in a 0.4 Pa (3 mTorr) Ar sputter gas environment [under 10 standard cubic centimeter per second (sccm) Ar flow], the Pt/Co/Ir SAF complex was grown under three different sputter gas conditions in each of the two sample series: (1) 6 mTorr Ar; (2) 6 mTorr Kr, and (3) 6 mTorr Xe; each under 20 sccm flow of the particular gas species. The compressed gas cylinders used in this study were of 99.9999% (Ar), 99.999% (Kr), and 99.999% (Xe) purity. Samples were grown at room temperature and measured in the as-deposited condition.

Distance from the center of the substrate to each sputtering gun was fixed at 20 cm with the target surface normal inclined 30° away from the substrate surface normal. Coincident with the pressure during deposition, the sample growth processing takes place under a 160 mm-Pa pressure−distance product, which improves the thermalization of sputtered atoms and to a lesser degree, backscattered ions as well.[37] Continuous azimuthal rotation of the substrate at 20 revolutions per minute was carried out during deposition except for during the Ir layer in order to generate a thickness gradient (wedge) across the substrate to explore Ir thicknesses in the vicinity of the thickness of the first anti-FM peak (≈0.45 nm) in Ir-based SAFs.[3,31] Figure 1b shows a schematic depiction of the wedge series A sample that depicts the oscillatory Ir thickness dependence[1] of the SAF magnetization orientation (depicted by the blue arrows in each Co/Pt multilayers) in our nanolayered structures: a thin Ir range, where the direct contact between Co layers induces mutual FM alignment; an intermediate Ir range, over which the two Co/Pt multilayers align anti-ferromagnetically (AF); and a thick Ir range, across which the two Co/Pt multilayers align FM. Film deposition rates and Ir lateral thickness variation were estimated by X-ray reflectivity of calibration films grown under identical pressure, gas flow, and substrate lateral size. The deposition rates are as follows: Ta (0.017 nm/s); Pt (0.020 nm/s); Co (0.015 nm/s); Ir (0.023 nm/s); Ru (0.029 nm/s) MgO (0.002 nm/s); Mo (0.021 nm/s) and CoFeB (0.024 nm/s). The average Ir thickness gradient across a 7 cm Si wafer ranged from 0.4 nm (Ar) to 0.5 nm (Kr), to 0.9 nm (Xe), permitting a wide range of Ir thicknesses to be explored in samples taken at 5 mm increments along the thickness gradient. An array of quartz crystal thickness monitors on either side of the substrate provided in situ confirmation of consistent deposition rates during growth of each layer of the samples compared to the deposition rates estimated from calibration films.

Magnetic properties were characterized using a quantum design superconducting quantum interference device (SQUID) magnetometer.[38] Both out-of-plane and in-plane magnetic hysteresis curves were measured using SQUID. Simulation of the energy distributions of ionized sputter gases reflected from the Co(Pt, Ir) sputter targets was carried out using the transport of ions in matter (TRIM) code.[39]

Cross-section transmission electron microscopy (TEM) images were acquired for each of the process gas conditions in series A, and exemplary high-resolution TEM images are shown in Figure 2a−c. Additional scanning TEM images in brightfield mode were used to refine our estimates for the film thickness and confirm the Ir thickness corresponding to the maximal IEC (see Supporting Information Section S1 for these details). All micrographs reveal smooth films with low interfaces under the processing conditions of 6 mTorr Ar (Kr, Xe) environments, including a well-defined interface at the Co/Ir/Co trilayer transition between the lower Co/Pt multilayers and the upper Co/Pt multilayers, key to realizing optimal IEC coupling across the sample. Oxidation of the Ta capping layer is apparent in each sample from the brightness and density of the layer in comparison to the Ta seed layer.

Compared to the Ar and Kr samples, the Xe sample exhibits the least amount of lattice distortions, suggesting better alignment of the (111) face-centered-cubic columnar grain growth of the multilayered film along the growth direction which has been seen previously in Xe-sputtered Co/Pt multilayers.[35] A countable number of grains in each TEM specimen (see additional TEM images in Supporting Information Section S1) enabled some feedback on grain sizes within series A, for which we observe grains as wide as 18 nm in the Ar and Xe samples, but below 14 nm in the Kr

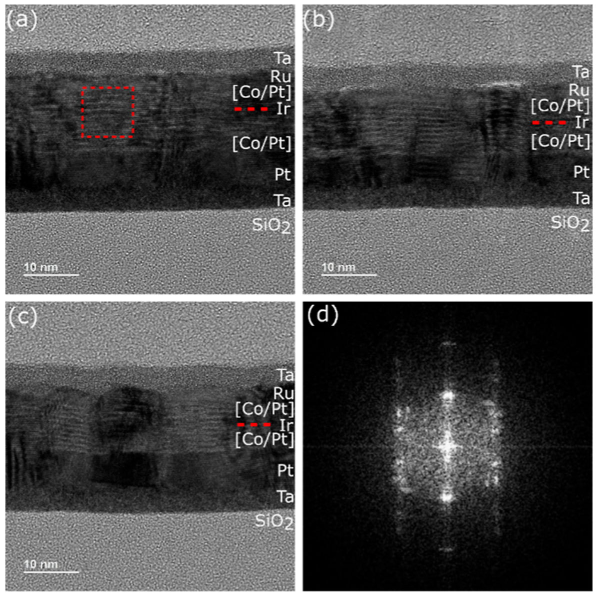

Figure 2. Cross-section TEM images of series A films grown in Ar (a), Kr (b), and Xe (c). (d) Two-dimensional fast Fourier transform diffractogram of enclosed region in (a).

sample. Within grains, the nanolayered stacking of Pt/Co/Ir multilayers within the SAF are continuous and discrete, with very low roughness across the nearly 10 nm span of most grains. A larger wavelength roughness associated with the competition during growth over the Pt-buffer can be seen across all three samples shown in Figure 2 and additionally in supplementary figures shown in Supporting Information Section S1. Atomic force micrographs (Supporting Information Figure S13) reveal a smooth surface roughness across the three samples in series A, with estimated root-mean-square roughness (R_q) values (0.44 ± 0.03) nm, (0.38 ± 0.01) nm, and (0.51 ± 0.05) for Ar, Kr, and Xe, respectively. Complementary information from specular X-ray reflectivity (Supporting Information Section S2) suggests a nearly 1 nm root-mean-squared roughness that develops from the Pt/Co/Ir SAF growth and is present at the Ru/Ta interface for each of the three sputtering gas conditions and is consistent with observations in the TEM micrographs. Smaller grains were misoriented relative to the (111)-textured columnar structure in the Co/Pt SAF and represent a distortion of the superlattice stacking. These distortions may generate additional orange-peel type coupling within each Co/Pt multilayers or between the two Co/Pt multilayers coupled across the Ir spacer that could influence the peak IEC.[40]

We use diffraction analysis to examine the lattice parameters in these three samples. Figure 2d shows an exemplary fast Fourier transform diffractogram from a region in the Ar sample highlighted in Figure 2a. The lattice spacing of the (111) planes in this region is 0.227 nm. For the Kr and Xe samples, the (111) lattice spacing was 0.224 nm. The larger out-of-plane lattice spacing within the Ar sample may be the consequence of in-plane compression from film bombardment during growth.[33] Additional X-ray diffraction in Supporting Information Section S2 shows the out-of-plane (111) texture of the nanolayered thin films and a significant increase in the mosaic spread of the (111) oriented crystallites in the progression from Ar to Kr to Xe, which may explain the increased coercivity in the films described below.

https://doi.org/10.1021/acsanm.2c03917
ACS Appl. Nano Mater. 2023, 6, 131−139

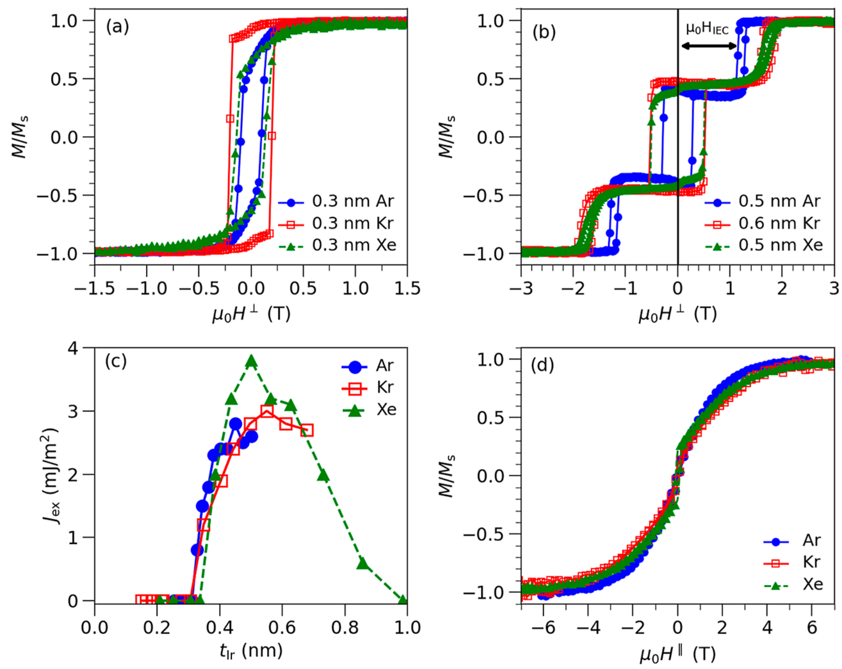

Figure 3. Magnetic hysteresis curves measured out-of-plane for series A samples using SQUID magnetometry for (a) 0.3 nm Ir thickness; (b) peak interlayer exchange field thickness; (c) interlayer exchange energy vs Ir thickness for series A; (d) magnetic hysteresis curves measured in-plane for samples in (b).

Table 1. Magnetic Properties Summary for Minimum Ir Spacer Thickness and Ir Thickness Associated with Maximum Interlayer Exchange Field for Series A and Series B for Each Sputtering Gas

series	gas	M_s (kA/m) ± 40 kA/m	t_{Ir} (nm)	$\mu_0 H_c$ (T) ± 0.025 T	$\mu_0 H_{IEC}$ (T) ± 0.025 T	J_{IEC} (mJ/m²)	$\mu_0 H_K$ (T) ± 0.05 T	K_{eff} (MJ/m³) = $1/2\mu_0 M s H_K$
A	Ar	590	0.3	0.100	FM	FM	1.80	0.53 ± 0.05
			0.5	0.275	1.325	2.7 ± 0.2	4.10	1.21 ± 0.06
	Kr	560	0.3	0.200	FM	FM	2.85	0.80 ± 0.06
			0.6	0.500	1.800	2.9 ± 0.2	4.95	1.40 ± 0.10
	Xe	850	0.3	0.150	FM	FM	2.25	0.96 ± 0.05
			0.5	0.500	1.925	3.8 ± 0.2	5.40	2.30 ± 0.10
B	Ar	760	0.3	0.050	FM	FM	1.70	0.65 ± 0.05
			0.5	0.300	0.725	1.9 ± 0.1	3.00	1.14 ± 0.08
	Kr	740	0.3	0.200	FM	FM	1.80	0.65 ± 0.05
			0.5	0.550	0.950	1.7 ± 0.2	3.35	1.24 ± 0.08
	Xe	960	0.3	0.150	FM	FM	1.60	0.77 ± 0.05
			0.5	0.500	0.975	2.1 ± 0.2	3.85	1.90 ± 0.10

Out-of-plane magnetization versus applied field hysteresis ($M-H$) curves were measured using a SQUID magnetometer for 5 mm × 5 mm cleaves taken from along the Ir thickness wedge in the series A samples. Figure 3a shows exemplary out-of-plane $M-H$ curves at approximately 0.3 nm Ir thickness, showing FM coupling between the two sets of Co/Pt multilayers. In addition to the hysteresis curves seen in Figure 3a and centered around zero field, samples that exhibit an anti-ferromagnetic IEC exhibit an additional pair of magnetic hysteresis loops that are shifted symmetrically around zero applied field, which can be seen in Figure 3b. The offset of the center of these shifted hysteresis loops from zero applied field is depicted by the arrow in Figure 3b and is defined as the IEC offset field, $\mu_0 H_{IEC}$. Despite the very high IEC field, nearly all of the $M-H$ loops with a measurably anti-FM coupling ridge additionally show coercivity in the IEC offset hysteresis loops (see Supporting Information Section S3), which may be a consequence of the large PMA in Pt/Co/Ir[31,32] or may additionally suggest alignment of the SAF through propagation of a vertical domain wall through the thicker Co/Pt (5 nm) multilayers into the thinner (3 nm) Co/Pt multilayers.[41] For an Ir thickness around 0.5 nm in each thickness series for Ar, Kr, and Xe, we observe the largest $\mu_0 H_{IEC}$ of (1.325 ± 0.025) T, (1.800 ± 0.025) T, and (1.925 ± 0.025) T, respectively, and the plus/minus quantity here and below reflects the one-sigma uncertainty in the measured parameter. The saturation magnetization for each of the Ar, Kr, and Xe samples in series A was (590 ± 40) kA/m, (560 ± 40) kA/m, and (850 ± 60) kA/m, respectively. The larger saturation magnetization for the Xe sample reflects a slightly higher ratio of Co-to-Pt compared to the nominal sample stacking structure and is consistent with observed Co and Pt thicknesses in the TEM micrographs (see Supporting Information Section S1). As summarized in Table 1, there are evident gains in both the peak IEC field and the coercive field at both high anti-FM IEC and low IEC, as evident for the Kr and Xe samples compared to the Ar sample

https://doi.org/10.1021/acsanm.2c03917
ACS Appl. Nano Mater. 2023, 6, 131−139

with a nearly 50% increase in the peak IEC field and an over 100% increase in the coercive field, consistent with previous studies of Co/Pt multilayers sputtered in Kr and Xe gas.

In-plane M−H curves for each gas in the series showing the maximum IEC field are shown in Figure 3d. All samples show a reversible in-plane hysteresis loop, consistent with a magnetic easy axis perpendicular to the film plane of the layers. The in-plane saturation field, H_s, reflects the anisotropy field (H_K) of the SAF, including contributions from the PMA at the Pt/Co and Ir/Co interfaces, the demagnetization field, and the IEC coupling field. The anisotropy field for Ar, Kr, and Xe samples with maximum anti-FM IEC was (3.00 ± 0.05) T, (3.35 ± 0.05) T and (3.85 ± 0.05) T, respectively, reaching the largest magnitudes for Kr and Xe, also consistent with previous studies of the role of Kr and Xe sputtering of Co/Pt multilayers. The anisotropy field for the corresponding samples with FM IEC was correspondingly lower by approximately one-half, in agreement with previous work that shows that IEC energy enhances the net PMA in Ir/Co/Pt pSAFs.[42] Table 1 shows that the difference for each sputtering gas between the anisotropy field for the peak IEC compared to the ultrathin Ir (t_{Ir} = 0.3 nm) spacer samples cannot be reconciled entirely by the interlayer exchange field strength, which points to the sensitivity of PMA to sub-nm thickness changes in the nanoscale Ir spacer layer.

The IEC field was estimated from each of the out-of-plane M−H hysteresis loops spanning the Ir thickness range of the wedge samples. Based on the saturation magnetization and the thickness of the [Co(0.4 nm)/Pt(0.6 nm)]$_{\times 3}$ (3 nm) component of the pSAF, we estimate the IEC energy as $J_{ex} = \mu_0 M_s H_{IEC} t$. Figure 3c shows the IEC energy versus nominal Ir thickness for each of the samples in the thickness series showing an anti-FM IEC offset in the out-of-plane M−H hysteresis loops. Due to the relatively steep thickness gradient across the full sample (0.4 nm across 70 mm), the measured 5 mm wide samples cover approximately the thickness stepsize between samples. Consistent with the gains in PMA and coercivity, we notice that the peak IEC energy is manifest in the Xe series, with a range of nominal thickness values showing larger IEC energies than the maximum IEC energy for Ar or Kr by 10% up to 30%. Typical IEC strength as a function of the Ir spacer thickness is very sensitive to the subnanolayer thickness,[31] which can be seen in the steep rise and beginning of rapid descent in the Ar sample, but not in the Kr and Xe samples. While we do see a steep rise in the IEC strength, the coupling falls off much less rapidly, which may be consistent with a surface-morphology mediated coupling. If the Kr(Xe)-sputtered SAFs develop more roughness, then the effective thickness of the Ir spacer layer will be lower than the nominal thickness and corrugation-induced magnetostatic coupling could deliver additional anti-FM coupling[43] in addition to IEC mediated through indirect exchange interactions across the Ir spacer. These values additionally exceed the leading 2.6 mJ/m^2 value recently observed in Ir/Co/Pt-based pSAFs.[31]

The structural and magnetic properties indicate that the pSAFs grown in an Ar environment compared to Kr or Xe not only exhibit better crystallinity and denser, more compressive films but also exhibit lower coercivity, PMA and IEC. The difference in microstructure is consistent with effects of ion bombardment and gains in PMA and coercivity have been correlated to ion bombardment during Pt sputtering in an Ar environment. To understand additionally how the full pSAF could be affected by ion bombardment during sputtering, we carried out TRIM calculations using 100,000 sputtering events to generate statistics for the energy of sputtered atoms (Co, Pt and Ir) and backscattered ions (Ar^+, Kr^+ and Xe^+) in each of the gas environments. For each simulation, we assume that the sputtering target bias is 350 V. Then we considered the energy lost due to scattering in the gas environment to estimate the energy arriving at the growing film.

The sputtered atoms depart their respective target with energies in the range of a few eV and would be expected to lose at least 90% of their initial energy during their transit through the gas environment, based on the pressure−distance product of the sputtering chamber (160 mm Pa).[37] As a consequence, we will not consider the effects of bombardment from sputtered atoms. On the other hand, backscattered ions from the sputtering gas reflect from the target with high energy and can maintain a significant fraction of their incident energy as they bombard the target. Energy loss arising from collisions between gas molecules using the same 160 mm Pa pressure distance, should reduce the arriving energy of the back-scattered ions in Ar by a factor of 2, in Kr by a factor of 10, and in Xe by a factor of 100.[37] Figure 4a highlights the arrival energy distribution of backscattered ions during Pt and Ir

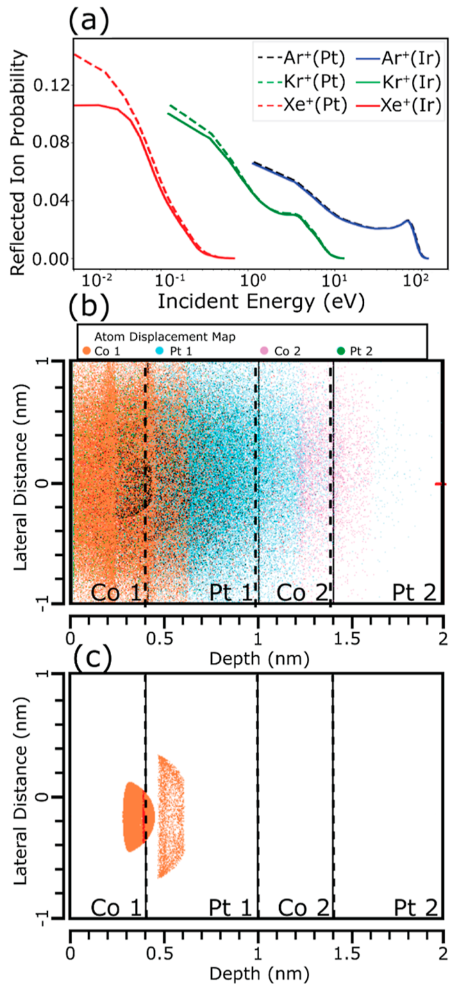

Figure 4. (a) Incident energy of arriving backscattered gas ions indicating sputter target in parentheses; (b) atomic displacement map due to 75 eV Ar^+ ions incident on [Co/Pt] multilayers during Ir or Pt deposition in 6 mTorr Ar; and (c) atomic displacement map due to 4 eV Kr^+ ions.

https://doi.org/10.1021/acsanm.2c03917
ACS Appl. Nano Mater. 2023, 6, 131−139

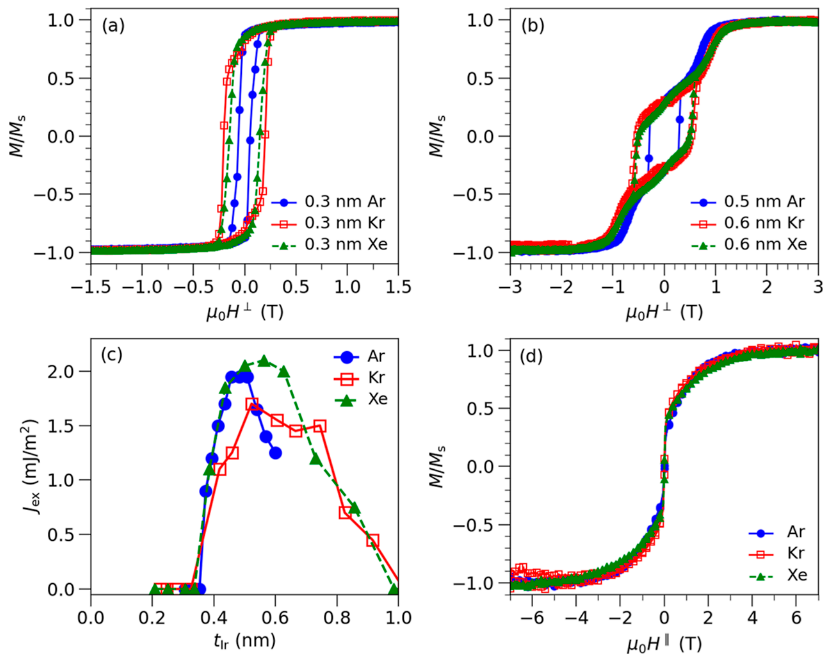

Figure 5. Exemplary out-of-plane M−H curves for MgO-buffered series B with (a) 0.3 nm Ir thickness; (b) peak interlayer exchange field thickness; and (c) interlayer exchange energy vs Ir thickness for series B; (d) in-plane M−H curves for MgO-buffered series B at peak interlayer exchange field thickness.

deposition based on TRIM simulations of 10,000 sputtering events with Pt (Ir) targets at normal incidence with 300 eV Ar^+ (Kr^+, Xe^+) ions.[39] We estimate an average incident energy at the substrate for Pt (Ir) of: 37 eV (38 eV) in 6 mTorr Ar; 3 eV (6 eV) in 6 mTorr Kr and 0.1 eV (0.3 eV) in 6 mTorr Xe, with tails of the Ar distribution in excess of 100 eV for both species. To illustrate the damage that the high-energy ions could produce, we simulated the atomic displacements in two Co/Pt bilayer repeats during the Ir deposition, assuming 75 eV incident Ar^+ ions reflected from the Ir target. Figure 4b shows significant displacement of the Co (Pt) atoms laterally and into the adjacent Pt (Co) layers under ion bombardment from backscattered Ar^+ ions. Our simulations additionally suggest that this damage would be constrained to a narrow region of the uppermost Co/Pt interface (Figure 4c) for Kr^+ sputtering and would be virtually nonexistent using the relevant energies for Xe^+ sputtering.

We now move on to the series B structure, the so-called top-pinned complex. The top-pinned pMTJ demands an abrupt structural transition from an amorphous CoFeB layer adjacent to the MgO tunnel barrier and an fcc(111) Co-based multilayer with only an ultrathin refractory metal (Ta or Mo or W) bridge layer instead of a thick Pt(111) buffer layer as was employed in series A. Figure 5a,b highlights the key out-of-plane M−H loops for series B, where again similarities in the appearance of wider coercive field are seen for the Kr- and Xe-grown samples compared to the Ar sample. Additional out-of-plane M−H loops for this sample are available in Supporting Information Section S4. The peak IEC energy (see Figure 5c) is also moderately higher for the Xe-grown films, consistent with our observations for the series A samples.

The peak IEC energies for series B are (1.9 ± 0.1) mJ/m^2, (1.7 ± 0.2) mJ/m^2, and (2.1 ± 0.2) mJ/m^2 for Ar, Kr, and Xe, respectively. The perpendicular magnetic anisotropy field ($\mu_0 H_K$) estimated from the in-plane magnetic saturation field (Figure 5d) reveals that the samples with the highest interlayer exchange in each gas series (see Table 1) also showed the largest PMA: (3.00 ± 0.05) T; (3.35 ± 0.05) T; and (3.85 ± 0.05) T for Ar, Kr, and Xe, respectively.

Recent efforts to cooptimize IEC with other functional properties in Ru/Co/Pt and Ir/Co/Pt multilayers have realized technologically significant benchmarks for ultrathin Co layers combined with well-controlled interfaces. In Lau et al., a series of Ir/Co/Pt and Pt/Co/Ir sputtered superlattices are examined in which they realize PMA fields approaching 10 T in a sample with an IEC field of approximately 3 T in an optimized structure of [Ir (0.45 nm)/Co (0.9 nm)/Pt(0.6 nm)]$_{\times 12}$.[42] Assuming a value for the saturation magnetization appropriate to this stacking structure (600 kA/m), this translates to a K_{eff} of approximately 3 MJ/m^3 and a J_{IEC} slightly below 1.5 mJ/m^2, which compares favorably with our values (K_{eff} = 2.3 MJ/m^3, J_{IEC} = 3.8 mJ/m^2) for the peak IEC Xe sample in series A. Also recently, Karayev et al. highlighted the cooptimization of IEC energy (1.3 mJ/m^2) in [Pt (1.0 nm)/Co (0.8 nm)/Ir (0.45 nm)]$_{\times 10}$ and [Pt (1.0 nm)/Co (0.8 nm)/Ru (0.95 nm)]$_{\times 10}$ superlattices[44] in superlattice materials already showing very high interfacial Dzyaloshinskii−Moriya interaction (DMI) energy (2.66 mJ/m^2) and moderate PMA (K_{eff} < 0.5 MJ/m^3).[45] Although our emphasis was on two Co/Pt superlattices coupled by a single Ir layer to convert IEC, these recent findings shed light on the alternative layer stacking structures (e.g. Ir/Co/Pt superlattices) that could deliver additional gains in PMA and DMI with the use of either Kr or Xe as the sputtering process gas.

Realizing magnetic multilayered films with high PMA and IEC requires judicious control of interface sharpness between each of the ultrathin layers comprising the layer stacking structure. Our results suggest that heavier sputter gas molecules such as Kr and Xe can improve these functional properties as their use leads to less energy being delivered to the growing film, both through deceleration of the sputtered constituent atoms and the reflected gas molecules. There may

https://doi.org/10.1021/acsanm.2c03917
ACS Appl. Nano Mater. 2023, 6, 131−139

be several microscopic mechanisms involved in the improved PMA and IEC. This may include reduced surface defects at the Pt/Co and Ir/Co interfaces, known to improve PMA in Fe(Co)/MgO-based interfacial anisotropy nanolayered systems.[46,47] Larger IEC in Kr(Xe)-sputtered films due to reduced intermixing at the Co/Ir/Co interface was explored in other systems (e.g., Fe/V multilayers[48]) and understood as a consequence of direct exchange (adjacent Co−Co) coupling that reduces the observed IEC strength. The described approach in this work has the potential to be compatible with industrial thin-film processes, provided that alternative process gases can be implemented in the deposition tool. Alternative approaches may be employed to reduce the energy of bombarding species at the growing film, including engineering a pressure−distance product for significant attenuation of initials sputtered atom and reflected ion energies.[37] It could alternatively be possible to employ a positive biasing of the substrate to mitigate reflected ions from bombarding the growing film.[49]

CONCLUSIONS

We have grown Ir-based SAFs using Ar, Kr, and Xe gas sputtering. Our results indicate that the heavier mass of Kr and Xe gas molecules lead to lower film stress, a higher degree of (111) texturing, and higher PMA and IEC for both Pt(111)-buffered and amorphous CoFeB/Mo-buffered films. Advantageously, the IEC realized in a Xe sputtering environment is over 30% higher than what has been previously realized by sputtering in a Ar environment, including our present work, pointing to the critical role of sputter gas species on the IEC and PMA of nanolayered perpendicular SAF structures. Moreover, this approach is compatible with growth on an amorphous MgO/CoFeB/Mo-buffer, signifying the utility of this processing technique for both bottom-pinned and top-pinned pMTJ memory devices.

ASSOCIATED CONTENT

Supporting Information

The Supporting Information is available free of charge at https://pubs.acs.org/doi/10.1021/acsanm.2c03917.

Additional scanning transmission electron micrographs, X-ray diffraction, atomic (and magnetic) force micrographs, and magnetic hysteresis loops (PDF)

AUTHOR INFORMATION

Corresponding Author

Daniel B. Gopman − *Materials Science and Engineering Division, National Institute of Standards and Technology, Gaithersburg, Maryland 20899, United States;* orcid.org/0000-0003-4172-8113; Email: daniel.gopman@nist.gov

Authors

Chloe S. Taylor − *Department of Physics, Harvey-Mudd College, Claremont, California 91711, United States; Materials Science and Engineering Division, National Institute of Standards and Technology, Gaithersburg, Maryland 20899, United States*

Marzieh Savadkoohi − *Materials Science and Engineering Division, National Institute of Standards and Technology, Gaithersburg, Maryland 20899, United States; School of Engineering and Applied Sciences, University of the District of Columbia, Washington, District of Columbia 20008, United States*

Pawan Tyagi − *School of Engineering and Applied Sciences, University of the District of Columbia, Washington, District of Columbia 20008, United States;* orcid.org/0000-0002-7541-1344

Jenae E. Shoup − *Materials Science and Engineering Division, National Institute of Standards and Technology, Gaithersburg, Maryland 20899, United States; Department of Physics, University of South Florida, Tampa, Florida 33620, United States*

Dario A. Arena − *Department of Physics, University of South Florida, Tampa, Florida 33620, United States;* orcid.org/0000-0001-7463-6472

Julie A. Borchers − *NIST Center for Neutron Research, National Institute of Standards and Technology, Gaithersburg, Maryland 20899, United States*

James Eckert − *Department of Physics, Harvey-Mudd College, Claremont, California 91711, United States*

Complete contact information is available at: https://pubs.acs.org/10.1021/acsanm.2c03917

Notes

The authors declare no competing financial interest.

ACKNOWLEDGMENTS

M.S. gratefully acknowledges the funding support from National Science Foundation-CREST award (contract no. HRD-1914751). J.E.S. and D.A.A. acknowledge the support of the National Science Foundation (NSF) under grant no. ECCS-1952957. C.S.T. acknowledges the support of the National Institute of Standards and Technology under the Summer Undergraduate Research Fellowship program.

REFERENCES

(1) Duine, R. A.; Lee, K.-J.; Parkin, S. S. P.; Stiles, M. D. Synthetic antiferromagnetic spintronics. *Nat. Phys.* **2018**, *14*, 217−219.

(2) Majkrzak, C. F.; Cable, J. W.; Kwo, J.; Hong, M.; McWhan, D. B.; Yafet, Y.; Waszczak, J. V.; Vettier, C. Observation of a Magnetic Antiphase Domain Structure with Long-Range Order in a Synthetic Gd-Y Superlattice. *Phys. Rev. Lett.* **1986**, *56*, 2700−2703.

(3) Parkin, S. S. P. Systematic variation of the strength and oscillation period of indirect magnetic exchange coupling through the 3d, 4d, and 5d transition metals. *Phys. Rev. Lett.* **1991**, *67*, 3598−3601.

(4) Unguris, J.; Celotta, R. J.; Pierce, D. T. Observation of two different oscillation periods in the exchange coupling of Fe/Cr/Fe(100). *Phys. Rev. Lett.* **1991**, *67*, 140−143.

(5) Bhatti, S.; Sbiaa, R.; Hirohata, A.; Ohno, H.; Fukami, S.; Piramanayagam, S. N. Spintronics based random access memory: a review. *Mater. Today* **2017**, *20*, 530−548.

(6) Krounbi, M.; Nikitin, V.; Apalkov, D.; Lee, J.; Tang, X.; Beach, R.; Erickson, D.; Chen, E. (Keynote) Status and Challenges in Spin-Transfer Torque MRAM Technology. *ECS Trans.* **2015**, *69*, 119−126.

(7) Inomata, K.; Nozaki, T.; Tezuka, N.; Sugimoto, S. Magnetic switching field and giant magnetoresistance effect of multilayers with synthetic antiferromagnet free layers. *Appl. Phys. Lett.* **2002**, *81*, 310−312.

(8) Cuchet, L.; Rodmacq, B.; Auffret, S.; Sousa, R. C.; Prejbeanu, I. L.; Dieny, B. Perpendicular magnetic tunnel junctions with a synthetic storage or reference layer: A new route towards Pt- and Pd-free junctions. *Sci. Rep.* **2016**, *6*, 21246.

(9) Zhang, D.-L.; Sun, C.; Lv, Y.; Schliep, K. B.; Zhao, Z.; Chen, J.-Y.; Voyles, P. M.; Wang, J.-P. L10 Fe-Pd Synthetic Antiferromagnet

through an fcc Ru Spacer Utilized for Perpendicular Magnetic Tunnel Junctions. *Phys. Rev. Appl.* **2018**, *9*, 044028.

(10) Cohen, A.; Jonville, A.; Liu, Z.; Garg, C.; Filippou, P. C.; Yang, S.-H. Current driven chiral domain wall motions in synthetic antiferromagnets with Co/Rh/Co. *J. Appl. Phys.* **2020**, *128*, 053902.

(11) Romming, N.; Hanneken, C.; Menzel, M.; Bickel, J. E.; Wolter, B.; von Bergmann, K.; Kubetzka, A.; Wiesendanger, R. Writing and Deleting Single Magnetic Skyrmions. *Science* **2013**, *341*, 636−639.

(12) Manchon, A.; Železný, J.; Miron, I. M.; Jungwirth, T.; Sinova, J.; Thiaville, A.; Garello, K.; Gambardella, P. Current-induced spin-orbit torques in ferromagnetic and antiferromagnetic systems. *Rev. Mod. Phys.* **2019**, *91*, 035004.

(13) Emori, S.; Bauer, U.; Ahn, S.-M.; Martinez, E.; Beach, G. S. D. Current-driven dynamics of chiral ferromagnetic domain walls. *Nat. Mater.* **2013**, *12*, 611−616.

(14) Ryu, K.-S.; Thomas, L.; Yang, S.-H.; Parkin, S. Chiral spin torque at magnetic domain walls. *Nat. Nanotechnol.* **2013**, *8*, 527−533.

(15) Yang, S.-H.; Ryu, K.-S.; Parkin, S. Domain-wall velocities of up to 750 m s−1 driven by exchange-coupling torque in synthetic antiferromagnets. *Nat. Nanotechnol.* **2015**, *10*, 221−226.

(16) Yang, S.-H.; Parkin, S. Novel domain wall dynamics in synthetic antiferromagnets. *J. Phys.: Condens. Matter* **2017**, *29*, 303001.

(17) Zhang, X.; Zhou, Y.; Ezawa, M. Magnetic bilayer-skyrmions without skyrmion Hall effect. *Nat. Commun.* **2016**, *7*, 10293.

(18) Nagaosa, N.; Tokura, Y. Topological properties and dynamics of magnetic skyrmions. *Nat. Nanotechnol.* **2013**, *8*, 899−911.

(19) Jiang, W.; Zhang, X.; Yu, G.; Zhang, W.; Wang, X.; Benjamin Jungfleisch, M.; Pearson, J. E.; Cheng, X.; Heinonen, O.; Wang, K. L.; Zhou, Y.; Hoffmann, A.; te Velthuis, S. G. E. Direct observation of the skyrmion Hall effect. *Nat. Phys.* **2017**, *13*, 162−169.

(20) Kent, A. D.; Worledge, D. C. A new spin on magnetic memories. *Nat. Nanotechnol.* **2015**, *10*, 187−191.

(21) Ikeda, S.; Miura, K.; Yamamoto, H.; Mizunuma, K.; Gan, H. D.; Endo, M.; Kanai, S.; Hayakawa, J.; Matsukura, F.; Ohno, H. A perpendicular-anisotropy CoFeB−MgO magnetic tunnel junction. *Nat. Mater.* **2010**, *9*, 721−724.

(22) Honjo, H.; Ikeda, S.; Sato, H.; Nishioka, K.; Watanabe, T.; Miura, S.; Nasuno, T.; Noguchi, Y.; Yasuhira, M.; Tanigawa, T.; Koike, H.; Inoue, H.; Muraguchi, M.; Niwa, M.; Ohno, H.; Endoh, T. Impact of Tungsten Sputtering Condition on Magnetic and Transport Properties of Double-MgO Magnetic Tunneling Junction With CoFeB/W/CoFeB Free Layer. *IEEE Trans. Magn.* **2017**, *53*, 2501604.

(23) Liu, T.; Cai, J. W.; Sun, L. Large enhanced perpendicular magnetic anisotropy in CoFeB/MgO system with the typical Ta buffer replaced by an Hf layer. *AIP Adv.* **2012**, *2*, 032151.

(24) Cai, W.; Cao, K.; Wang, M.; Peng, S.; Zhou, J.; Cao, A.; Zhang, B.; Wang, L.; Zhang, Y.; Wei, J.; He, X.; Cui, H.; Zhao, C.; Zhao, W. In Interfacial Property Tuning of Heavy metal/CoFeB for Large Density STT-MRAM. *2017 17th Non-volatile Memory Technology Symposium (NVMTS)*; IEEE, 2017; pp 1−4, 30 Aug.-1 Sept. 2017. DOI: 10.1109/nvmts.2017.8171303

(25) Santos, T. S.; Mihajlović, G.; Smith, N.; Li, J.-L.; Carey, M.; Katine, J. A.; Terris, B. D. Ultrathin perpendicular free layers for lowering the switching current in STT-MRAM. *J. Appl. Phys.* **2020**, *128*, 113904.

(26) Carcia, P. F.; Meinhaldt, A. D.; Suna, A. Perpendicular magnetic anisotropy in Pd/Co thin film layered structures. *Appl. Phys. Lett.* **1985**, *47*, 178−180.

(27) Carcia, P. F. Perpendicular magnetic anisotropy in Pd/Co and Pt/Co thin-film layered structures. *J. Appl. Phys.* **1988**, *63*, 5066−5073.

(28) Chen, P. J.; Iunin, Y. L.; Cheng, S. F.; Shull, R. D. Underlayer Effect on Perpendicular Magnetic Anisotropy in Co20Fe60B20/MgO Films. *IEEE Trans. Magn.* **2016**, *52*, 1−4.

(29) Nakamura, N.; Ogi, H.; Hirao, M.; Ono, T. Elastic constants and magnetic anisotropy of Co/Pt superlattice thin films. *Appl. Phys. Lett.* **2005**, *86*, 111918.

(30) Omelchenko, P.; Heinrich, B.; Girt, E. Measurements of interlayer exchange coupling of Pt in Py|Pt|Py system. *Appl. Phys. Lett.* **2018**, *113*, 142401.

(31) Yakushiji, K.; Sugihara, A.; Fukushima, A.; Kubota, H.; Yuasa, S. Very strong antiferromagnetic interlayer exchange coupling with iridium spacer layer for perpendicular magnetic tunnel junctions. *Appl. Phys. Lett.* **2017**, *110*, 092406.

(32) Huai, Y.; Gan, H.; Wang, Z.; Xu, P.; Hao, X.; Yen, B. K.; Malmhall, R.; Pakala, N.; Wang, C.; Zhang, J.; Zhou, Y.; Jung, D.; Satoh, K.; Wang, R.; Xue, L.; Pakala, M. High performance perpendicular magnetic tunnel junction with Co/Ir interfacial anisotropy for embedded and standalone STT-MRAM applications. *Appl. Phys. Lett.* **2018**, *112*, 092402.

(33) Winters, H. F.; Coufal, H. J.; Eckstein, W. Influence of energy reflected from the target on thin film characteristics. *J. Vac. Sci. Technol., A* **1993**, *11*, 657−663.

(34) Carcia, P. F.; Shah, S. I.; Zeper, W. B. Effect of energetic bombardment on the magnetic coercivity of sputtered Pt/Co thin-film multilayers. *Appl. Phys. Lett.* **1990**, *56*, 2345−2347.

(35) Carcia, P. F.; Li, Z. G.; Zeper, W. B. Effect of sputter-deposition processes on the microstructure and magnetic properties of Pt/Co multilayers. *J. Magn. Magn. Mater.* **1993**, *121*, 452−460.

(36) McMorran, B. J.; Cochran, A. C.; Dumas, R. K.; Liu, K.; Morrow, P.; Pierce, D. T.; Unguris, J. Measuring the effects of low energy ion milling on the magnetization of Co/Pd multilayers using scanning electron microscopy with polarization analysis. *J. Appl. Phys.* **2010**, *107*, 09D305.

(37) Somekh, R. E. The thermalization of energetic atoms during the sputtering process. *J. Vac. Sci. Technol., A* **1984**, *2*, 1285−1291.

(38) Certain commercial equipment, instruments, or materials are identified in this paper in order to specify the experimental procedure adequately. Such identification is not intended to imply recommendation or endorsement by NIST, nor is it intended to imply that the materials or equipment identified are necessarily the best available for the purpose.

(39) Ziegler, J. F.; Ziegler, M. D.; Biersack, J. P. SRIM—The stopping and range of ions in matter (2010). *Nucl. Instrum. Methods Phys. Res., Sect. B* **2010**, *268*, 1818−1823.

(40) Moritz, J.; Garcia, F.; Toussaint, J. C.; Dieny, B.; Nozières, J. P. Orange peel coupling in multilayers with perpendicular magnetic anisotropy: Application to (Co/Pt)-based exchange-biased spin-valves. *Europhys. Lett.* **2004**, *65*, 123−129.

(41) Folkerts, W.; Purcell, S. T. Antiferromagnetically coupled multilayer systems: magnetization curves in the case of unequal thicknesses of the magnetic layers. *J. Magn. Magn. Mater.* **1992**, *111*, 306−312.

(42) Lau, Y.-C.; Chi, Z.; Taniguchi, T.; Kawaguchi, M.; Shibata, G.; Kawamura, N.; Suzuki, M.; Fukami, S.; Fujimori, A.; Ohno, H.; Hayashi, M. Giant perpendicular magnetic anisotropy in Ir/Co/Pt multilayers. *Phys. Rev. Mater.* **2019**, *3*, 104419.

(43) Moritz, J.; Garcia, F.; Toussaint, J. C.; Dieny, B.; Nozières, J. P. Orange peel coupling in multilayers with perpendicular magnetic anisotropy: Application to (Co/Pt)-based exchange-biased spin-valves. *Europhys. Lett.* **2004**, *65*, 123.

(44) Karayev, S.; Murray, P. D.; Khadka, D.; Thapaliya, T. R.; Liu, K.; Huang, S. X. Interlayer exchange coupling in Pt/Co/Ru and Pt/Co/Ir superlattices. *Phys. Rev. Mater.* **2019**, *3*, 041401.

(45) Khadka, D.; Karayev, S.; Huang, S. X. Dzyaloshinskii−Moriya interaction in Pt/Co/Ir and Pt/Co/Ru multilayer films. *J. Appl. Phys.* **2018**, *123*, 123905.

(46) Yang, H. X.; Chshiev, M.; Dieny, B.; Lee, J. H.; Manchon, A.; Shin, K. H. First-principles investigation of the very large perpendicular magnetic anisotropy at Fe$|$MgO and Co$|$MgO interfaces. *Phys. Rev. B: Condens. Matter Mater. Phys.* **2011**, *84*, 054401.

(47) Hallal, A.; Yang, H. X.; Dieny, B.; Chshiev, M. Anatomy of perpendicular magnetic anisotropy in Fe/MgO magnetic tunnel junctions: First-principles insight. *Phys. Rev. B: Condens. Matter Mater. Phys.* **2013**, *88*, 184423.

(48) Schwickert, M. M.; Coehoorn, R.; Tomaz, M. A.; Mayo, E.; Lederman, D.; O'Brien, W. L.; Lin, T.; Harp, G. R. Magnetic moments, coupling, and interface interdiffusion in Fe/V(001) superlattices. *Phys. Rev. B: Condens. Matter Mater. Phys.* **1998**, *57*, 13681−13691.
(49) Zeng, G.-S.; Liu, C.-L.; Chen, S.-H. Effect of Substrate Biasing on the Epitaxial Growth and Structural Properties of RF Magnetron Sputtered Germanium Buffer Layer on Silicon. *Coatings* **2021**, *11*, 1060.

https://doi.org/10.1021/acsanm.2c03917
ACS Appl. Nano Mater. 2023, 6, 131−139